

## Multi-Frequency Synthesis of VLBI Images Using a Generalized Maximum Entropy Method

A. T. Bajkova

*Main Astronomical Observatory, Russian Academy of Sciences  
Pulkovo, St.Petersburg, 196140 Russia*

Received February 26, 2008; in final form, July 2, 2008

**Abstract** – A new multi-frequency synthesis algorithm for reconstructing images from multi-frequency VLBI data is proposed. The algorithm is based on a generalized maximum-entropy method, and makes it possible to derive an effective spectral correction for images over a broad frequency bandwidth, while simultaneously reconstructing the spectral-index distribution over the source. The results of numerical simulations demonstrating the capabilities of the algorithm are presented.

PACS numbers: 95.55.Jz, 95.75.Kk, 95.75.Mn

DOI: 10.1134/S1063772908120019

### 1. INTRODUCTION

Coverage of the  $UV$  spatial-frequency plane in VLBI observations [1] is mainly achieved using (1) several antennas, (2) the diurnal rotation of the Earth, (3) relocation of the antennas. However, the interferometer aperture is never filled completely due to the limited observation time and number of antennas, interruptions during the observations, and limitations on the smallest and longest baselines. Since the baseline coordinates  $U$  and  $V$  in the visibility function are measured in wavelengths, an alternative method of filling the  $UV$  plane is to observe a source at several frequencies simultaneously.

This method for fast filling of the aperture is called multi-frequency synthesis (MFS), and its effect is greatest in the case of interferometers with relatively few baselines. Figure 1a shows an example of a poor filling of the  $UV$  plane obtained by a four-element interferometer during 12 h of observations of a radio source with a declination of 34. at 8.2 GHz. The coordinates of the four telescopes were taken to be those of the three stations in the Russian QUASAR VLBI complex Svetloe, Zelenchukskaya, and Badary [2], together with the Matera station. Figures 1b, 1c, and 1d present the filling of the  $UV$  plane for MFS observations of this same source with this interferometer using various frequency ranges. Since the coordinates of the interferometer baseline are proportional to the frequency, different frequencies within the total band refer to different, radially arranged ( $U, V$ ) points. As we can see, MFS can provide a much denser filling of the  $UV$  plane, as well as increase the diameter of the synthesized aperture compared to the single frequency observations.

However, the application of MFS is complicated by the fact that the source brightness is a function of frequency; to avoid imaging artifacts due to this frequency dependence, we must derive and apply a spectral correction for the maps as they are deconvolved (reconstructed).

This problem has been considered by many authors. The most fundamental results on spectral effects in images and methods for correcting them are presented in [37]. These show that, when sufficiently narrow frequency bands are used, with widths within  $\pm 12.5\%$  of the reference frequency, we can essentially disregard the spectral dependence of the source brightness, since these effects are small and can be corrected for during calibration or self-calibration. However, for broader bands, e.g.,  $\pm 30\%$ , correction for spectral effects is necessary.

The most studied linear spectral-correction algorithm is based on the CLEAN method [8], and is called "double deconvolution" [3]. This algorithm involves the successive deconvolution of a "dirty" image using a "dirty" beam and using the beam corresponding to the spectral term. The development of this method enabling the simultaneous reconstruction of the desired image and the corresponding spectral map was proposed in [5]. The vector-relaxation algorithm [9] represents a generalized CLEAN deconvolution that can take into account spectral terms of any order.

An alternative deconvolution method that is also actively used in radio astronomy is the maximum entropy method (MEM). MEM was first proposed in [10] and [11] for the reconstruction of images in the optical and radio, respectively. Since then the method has been developed in many studies [12–18] and implemented in a number of software packages designed for image reconstruction (MEMSYS, AIPS, VLBIImager, etc.). A comparative analysis of CLEAN and MEM in VLBI is given in [16]; essentially, these methods complement each other. In particular, CLEAN is preferential for reconstructing images of compact sources from relatively poor data, while MEM is more suitable for imaging extended sources from better-quality data. A severe drawback of MEM compared to CLEAN, the bias of the solution [16], can easily be removed by generalizing the method to enable the reconstruction of sign-variable functions [17, 18]. This generalized MEM also enables difference imaging making it possible to substantially broaden the dynamic range of maps of sources including both compact and extended, faint components [19]. An important technical advantage of MEM over CLEAN is the absence of the need to discretize (grid) [1] the visibility function: MEM does not involve calculation of the inverse Fourier transform of the visibility data.

The purpose of the current study was to realize in an effective MFS aperture-synthesis method all the advantages of MEM, in order to enable high precision correction for spectral effects in a broad frequency band, as well as to study the developed algorithm for broad ranges of the various parameters involved.

## 2. SPECTRAL DEPENDENCE

The dependence of the source intensity on the frequency for synchrotron emission is usually described using the relation [37]

$$I(\nu) = I(\nu_0) \left( \frac{\nu}{\nu_0} \right)^\alpha, \quad (1)$$

where  $I(\nu_0)$  is the intensity at the reference frequency  $\nu_0$  and  $\alpha$  is the spectral index. For simplicity, we will use the notation  $I_0 = I(\nu_0)$ .

Restricting our consideration to the first  $Q$  terms of the Taylor expansion (1) at the point  $\nu_0$ , we can write the approximate equality

$$I(\nu) \approx I_0 + \sum_{q=1}^{Q-1} I_q \left( \frac{\nu - \nu_0}{\nu_0} \right)^q, \quad (2)$$

where

$$I_q = I_0 \frac{\alpha(\alpha - 1) \cdots [\alpha - (q - 1)]}{q!}.$$

In accordance with (2), we have for each point  $(l, m)$  in the two-dimensional  $(N \times N)$  brightness distribution (image, map) of the source

$$I(l, m) \approx I_0(l, m) + \sum_{q=1}^{Q-1} I_q(l, m) \left( \frac{\nu - \nu_0}{\nu_0} \right)^q, \quad (3)$$

where  $l, m = 1, \dots, N$ .

Thus, the obtained brightness distribution of the source (3) represents the sum of the brightness distribution at the reference frequency  $\nu_0$  and various spectral terms. The  $q$ th-order spectral map depends on the spectral-index distribution in the source as

$$I_q(l, m) = I_0(l, m) \frac{\alpha(l, m)[\alpha(l, m) - 1] \cdots [\alpha(l, m) - (q - 1)]}{q!}. \quad (4)$$

The first-order spectral map,

$$I_1(l, m) = I_0(l, m)\alpha(l, m) \quad (5)$$

is of primary interest.

We can obtain from (5) the estimate of the spectral index distribution in the source

$$\alpha(l, m) = I_1(l, m)/I_0(l, m). \quad (6)$$

### 3. RESTRICTIONS ON THE VISIBILITY FUNCTION

The complex visibility function represents the Fourier transform of the source intensity distribution, which satisfies the spectral dependence (1) at each point  $(l, m)$  of the map. In view of the finite order of the Taylor series expansion (3), we can write the restrictions on the visibility function as

$$V_{u_\nu, v_\nu} = \mathbf{F}\{I(l, m)\} \times \mathbf{D}_{u_\nu, v_\nu} \approx \sum_{q=0}^{Q-1} \mathbf{F} \left\{ I_q(l, m) \left( \frac{\nu - \nu_0}{\nu_0} \right)^q \right\} \times \mathbf{D}_{u_\nu, v_\nu}, \quad (7)$$

where  $\mathbf{F}$  denotes the Fourier transform and  $\mathbf{D}$  is the transfer function, which is a  $\delta$  function of  $u$  and  $v$  for each visibility measurement; each used frequency corresponds to its own set of  $\delta$  functions, indicated by the subscripts of  $u$  and  $v$ .

Let us rewrite (7) for the real and imaginary parts of the visibility function  $V_{u_\nu, v_\nu} = A_{u_\nu, v_\nu} + jB_{u_\nu, v_\nu}$  taking into account the measurement errors:

$$\sum_{q=0}^{Q-1} \sum_{l,m} I_q(l, m) a_{u_\nu, v_\nu}^{lm} \left( \frac{\nu - \nu_0}{\nu_0} \right)^q + \eta_{u_\nu, v_\nu}^{re} = A_{u_\nu, v_\nu}, \quad (8)$$

$$\sum_{q=0}^{Q-1} \sum_{l,m} I_q(l, m) b_{u_\nu, v_\nu}^{lm} \left( \frac{\nu - \nu_0}{\nu_0} \right)^q + \eta_{u_\nu, v_\nu}^{im} = B_{u_\nu, v_\nu}, \quad (9)$$

where  $a_{u_\nu, v_\nu}^{lm}$  and  $b_{u_\nu, v_\nu}^{lm}$  are constant factors (cosines and sines) that correspond to the Fourier transform;  $\eta_{u_\nu, v_\nu}^{re}$  and  $\eta_{u_\nu, v_\nu}^{im}$  are the real and imaginary parts of the additive instrumental noise, which has a normal distribution with zero mean and a known dispersion  $\sigma_{u_\nu, v_\nu}$ .

#### 4. RECONSTRUCTION METHOD

In our case, the unknowns are the distributions  $I_q(l, m)$  ( $q = 0, \dots, Q-1$ ;  $l, m = 1, \dots, N$ ) and the errors of the visibility function  $\eta_{u_\nu, v_\nu}^{re}$ ,  $\eta_{u_\nu, v_\nu}^{im}$ . Note that, in spite of the fact that the source brightness distribution is described by a nonnegative function, in general, spectral maps of arbitrary order (4) can take on both positive and negative values, due to the sign-variable spectral-index distribution in the source. Since the logarithm of a negative value is not defined on the set of real numbers, we will compose for the purpose of finding a solution for  $I_q(l, m)$ ,  $q = 0, \dots, Q-1$  a functional in which the values of the spectral maps are represented by their absolute values:

$$\mathbf{E} = \left\{ \sum_{l,m} I_0(l, m) \ln[I_0(l, m)] + \sum_{q=1}^{Q-1} \sum_{l,m} |I_q(l, m)| \ln[|I_q(l, m)|] \right\} + \rho \sum_{u_\nu, v_\nu} \frac{(\eta_{u_\nu, v_\nu}^{re})^2 + (\eta_{u_\nu, v_\nu}^{im})^2}{\sigma_{u_\nu, v_\nu}^2}, \quad (10)$$

$$I_0(l, m) \geq 0, \quad (11)$$

where  $\rho$  is a positive weighting coefficient.

The minimization of the functional (10) with the restrictions (8), (9), and (11) is the essence of MEM.

We can see from (10) that the minimized functional has two parts: the entropy functional in the Shannon form and a term representing an estimate of the 2 residual for the difference between the reconstructed spectrum and the data. This term can be considered an additional regularizing or stabilizing term that facilitates further regularization of the solution beyond that possible with the entropy functional alone [18]. We will bear in mind the effect of this term on the resolving power of the reconstruction algorithm.

For carrying out the reconstruction in practice, we now proceed to the generalized maximum-entropy method described in detail in [1719]. This consists in the substitution

$$I_q(l, m) = I_q^+(l, m) - I_q^-(l, m), \quad (12)$$

where the superscripts + and - denote the positive and negative parts of the function, and, in the following modification of functional (10),

$$\begin{aligned} \mathbf{E} = & \sum_{l,m} I_0(l, m) \ln[aI_0(l, m)] + \sum_{q=1}^{Q-1} \sum_{l,m} \{ I_q^+(l, m) \ln[aI_q^+(l, m)] + \\ & + I_q^-(l, m) \ln[aI_q^-(l, m)] \} + \rho \sum_{u_\nu, v_\nu} \frac{(\eta_{u_\nu, v_\nu}^{re})^2 + (\eta_{u_\nu, v_\nu}^{im})^2}{\sigma_{u_\nu, v_\nu}^2}, \end{aligned} \quad (13)$$

$$I_0(l, m) \geq 0, \quad I_q^+(l, m) \geq 0, \quad I_q^-(l, m) \geq 0, \quad (14)$$

where  $a \gg 1$  is a parameter responsible [as will be shown below, see (24)] for the accuracy with which the positive  $I_q^+(l, m)$  and negative  $I_q^-(l, m)$  parts of the solution for  $I_q(l, m)$  can be separated [see (12)].

The linear restrictions (8) and (9) on the visibility data are accordingly rewritten

$$\mathbf{R}_A = \sum_{l,m} I_0(l, m) a_{u_\nu, v_\nu}^{lm} + \sum_{q=1}^{Q-1} \sum_{l,m} [I_q^+(l, m) - I_q^-(l, m)] a_{u_\nu, v_\nu}^{lm} \left( \frac{\nu - \nu_0}{\nu_0} \right)^q + \eta_{u_\nu, v_\nu}^{re} = A_{u_\nu, v_\nu}, \quad (15)$$

$$\mathbf{R}_B = \sum_{l,m} I_0(l, m) b_{u_\nu, v_\nu}^{lm} + \sum_{q=1}^{Q-1} \sum_{l,m} [I_q^+(l, m) - I_q^-(l, m)] b_{u_\nu, v_\nu}^{lm} \left( \frac{\nu - \nu_0}{\nu_0} \right)^q + \eta_{u_\nu, v_\nu}^{im} = B_{u_\nu, v_\nu}, \quad (16)$$

where  $\mathbf{R}_A$  and  $\mathbf{R}_B$  denote the left-hand sides of the equations.

Thus, the reconstruction of the image  $I_0(l, m)$  requires the optimization of the functional (13); i.e., we must find

$$\min \mathbf{E} \quad (17)$$

with the constraints (14)(16) with respect to all the unknowns  $I_0(l, m)$ ,  $I_q^{+(-)}(l, m)$ ,  $q = 1, \dots, Q - 1$ ,  $l, m = 1, \dots, N$ , and  $\eta_{u_\nu, v_\nu}^{re}$ ,  $\eta_{u_\nu, v_\nu}^{im}$ . Note that the requirements (14) can be omitted since the entropy solution can only be positive; there then remain only the linear constraints (15) and (16) on the measurements of the complex visibility function.

## 6. THE OPTIMIZATION

The numerical solution for the optimization of (17) with the constraints (15) and (16) is based on the method of Lagrange multipliers; in this method, the conditional optimization is reduced to an unconditional optimization by composing the following dual functional, which is called the Lagrange functional:

$$\mathbf{L} = \mathbf{E} + \sum_{u_\nu, v_\nu} \{ \beta_{u_\nu, v_\nu} (\mathbf{R}_A - A_{u_\nu, v_\nu}) + \gamma_{u_\nu, v_\nu} (\mathbf{R}_B - B_{u_\nu, v_\nu}) \}, \quad (18)$$

where  $\beta_{u_\nu, v_\nu}$  and  $\gamma_{u_\nu, v_\nu}$  are Lagrange multipliers, or the dual variables with which the constraints (15) and (16) enter the considered functional.

Thus, the reconstruction is reduced to minimizing the Lagrange functional:

$$\min \mathbf{L}. \quad (19)$$

We optimize (19) using the necessary condition for the existence of an extremum:

$$\frac{d\mathbf{L}}{dI_0(l, m)} = 0; \quad \frac{d\mathbf{L}}{dI_q^+(l, m)} = 0; \quad \frac{d\mathbf{L}}{dI_q^-(l, m)} = 0$$

for  $q = 1, \dots, Q - 1$  and  $l, m = 1, \dots, N$ , and also

$$\frac{d\mathbf{L}}{d\eta_{u_\nu, v_\nu}^{re}} = 0; \quad \frac{d\mathbf{L}}{d\eta_{u_\nu, v_\nu}^{im}} = 0$$

for all values of the visibility function.

Note that a sufficient condition for the existence of a minimum of  $\mathbf{L}$  is the positive definiteness of the Hessian matrix.

As a result we obtain the following solution s for the required unknowns expressed in terms of the dual variables:

$$I_0(l, m) = \exp\left(- \sum_{u_\nu, v_\nu} [\beta_{u_\nu, v_\nu} a_{u_\nu, v_\nu}^{lm} + \gamma_{u_\nu, v_\nu} b_{u_\nu, v_\nu}^{lm}] - 1 - \ln a\right), \quad (20)$$

$$I_q^+(l, m) = \exp\left(- \sum_{u_\nu, v_\nu} [\beta_{u_\nu, v_\nu} a_{u_\nu, v_\nu}^{lm} + \gamma_{u_\nu, v_\nu} b_{u_\nu, v_\nu}^{lm}] \left(\frac{\nu - \nu_0}{\nu_0}\right)^q - 1 - \ln a\right), \quad (21)$$

$$I_q^-(l, m) = \exp\left(\sum_{u_\nu, v_\nu} [\beta_{u_\nu, v_\nu} a_{u_\nu, v_\nu}^{lm} + \gamma_{u_\nu, v_\nu} b_{u_\nu, v_\nu}^{lm}] \left(\frac{\nu - \nu_0}{\nu_0}\right)^q - 1 - \ln a\right), \quad (22)$$

$$\eta_{u_\nu, v_\nu}^{re} = -\frac{\sigma_{u_\nu, v_\nu}^2 \beta_{u_\nu, v_\nu}}{\rho}, \quad \eta_{u_\nu, v_\nu}^{im} = -\frac{\sigma_{u_\nu, v_\nu}^2 \gamma_{u_\nu, v_\nu}}{\rho}. \quad (23)$$

The solutions (20)(22) are exclusively positive. To obtain spectral maps, we must use (12).

It follows from (21) and (22) that the positive and negative parts of the spectral maps are related as

$$I_q^+(l, m)I_q^-(l, m) = \exp(-2 - 2 \ln a) = K(a), \quad (24)$$

with, as was said above, the parameter  $a$  playing the role of a separator between the positive and negative parts of the  $I_q(l, m)$  solution. The higher the value of  $a$ , the more exact the separation. The upper limit of  $a$  is determined by computational effects.

It can be readily shown that the Hessian matrix is positively defined everywhere; therefore, the functional  $\mathbf{L}$  is convex and the solution is global, i.e., unique.

Substituting the solutions (20)(23) in to the right-hand side of (18), we obtain the expression for the dual functional

$$\mathbf{L} = \sum_{l, m} I_0(l, m) + \sum_{q=1}^{Q-1} \sum_{l, m} [I_q^+(l, m) + I_q^-(l, m)] + \sum_{u_\nu, v_\nu} [\beta_{u_\nu, v_\nu} A_{u_\nu, v_\nu} + \gamma_{u_\nu, v_\nu} B_{u_\nu, v_\nu}], \quad (25)$$

Minimizing this expression [with regard to (20)(22)] enables us to find the dual variables  $\beta_{u_\nu, v_\nu}$  and  $\gamma_{u_\nu, v_\nu}$ .

We can find the extremum of (25) using various gradient methods. We utilized the coordinate-descent method, considering it to be the most reliable, though not the fastest. In this method, the increment of  $z_x$  for each unknown  $(\beta_{u_\nu, v_\nu}, \gamma_{u_\nu, v_\nu})$ , which we will conditionally denote  $x$ , is searched for based on the condition for an extremum of  $\mathbf{L}(z_x)$ :

$$\frac{d\mathbf{L}(z_x)}{dz_x} = 0. \quad (26)$$

$\mathbf{L}(z_x)$  is obtained by replacing the variable  $x$  in the functional  $\mathbf{L}$  (26) with  $x + z_x$ .

In our case, (25) is nonlinear in  $z_x$ . Obtaining a numerical solution using the Newton method is an iterative process. At the  $i$ th iteration, the value of  $z_x$  is

$$z_x^i = z_x^{i-1} - \left( d\mathbf{L}(z_x)/dz_x \right) / \left( d^2\mathbf{L}(z_x)/dz_x^2 \right) \Big|_{z_x=z_x^{i-1}}.$$

The solution for  $z_x$  usually converges after one to three iterations. As a result of one descent, the required variable acquires a new value,  $x + z_x$ . Simulation have shown that a high-quality reconstruction of the radio image and spectral maps requires from 100 to 500 descents in all dual coordinates  $\beta_{u_\nu, v_\nu}, \gamma_{u_\nu, v_\nu}$ .

## 5. SIMULATION RESULTS

In this section, we present the results of our numerical modeling of MFS using the above reconstruction based on the generalized MEM.

As a model radio source at frequency  $\nu_0$ , we consider the intensity distribution  $I_0(x, y)$  for two Gaussian components with amplitudes of 1 and 0.4 Jy/beam (Fig. 2a). The source size is about 3 4 mas in both right ascension and declination. Thus, the source has a size appropriate for VLBI mapping. The model spectral-index distribution of the source  $\alpha(x, y)$  is shown in Fig. 2c.

The model spectral indices have values from 0 to 0.84. The distribution of the first-order spectral map,  $I_1(x, y) = I_0(x, y)\alpha(x, y)$ , is shown in Fig. 2b. According to (4), odd-order spectral maps are positive and even-order spectral maps are negative. The sign of the model spectral-index distribution is not of primary importance from the viewpoint of testing the algorithm, since the solutions for the spectral maps of any order are searched for in the form of sign-variable functions [see (13) and (25)], and obtaining either positive or negative solutions is equally valid.

The contour levels in all images in Figs. 26 are 0.0625, 0.125, 0.25, 0.5, 1, 2, 4, 8, 16, 32, 64, and 99% of the peak value; this allows us to adequately display maps with dynamic ranges of up to 3200.

The visibility data are formed from the Fourier transform of the source intensity distribution calculated at each point  $(x, y)$  in accordance with the spectral dependence (1), with measurement errors added in accordance with (8) and (9).

We adopted  $\nu_0 = 8.2$  GHz as the central, or reference, frequency of the observations.

To study the quality of the synthesized images as a function of the range of frequencies used, we carried out simulations for three cases, with bandwidths of  $\pm 30\%$ ,  $\pm 60\%$ , and  $\pm 90\%$  of the central frequency. In each case, we used nine equidistant frequencies. The corresponding UV plane coverages are shown in Fig. 1.

The primary goal of our simulations is to analyze the quality of the image reconstruction using various degrees of spectral corrections, and to establish the minimum necessary number of spectral terms that must be included in the Taylor series (3) as a function of the frequency band used. We carried out this analysis first for fairly accurately measured visibility data (with a signal-to-noise ratio of about 100) and then for data containing appreciable measurement errors having a normal distribution with zero mean and a dispersion yielding a signal-to-noise ratio of about 10. We chose fairly broad frequency ranges (up to  $\pm 90\%$  of the central frequency) in order to more fully study the properties and capabilities of the developed frequency-correction algorithm, which is of considerable theoretical interest.

As was said in the Introduction, the idea of MFS arises in connection with the need for fast aperture image synthesis, and is most urgent for VLBI arrays with relatively few baselines (Fig. 1a). Figure 3a shows an image reconstructed from visibility data corresponding to the single-frequency coverage of the UV plane shown in Fig. 1a. Comparing the result of the reconstruction with the original image, we note severe distortions of the source shape, as well as some spurious features, leading to a low dynamic range for the derived map.

The MFS in a  $\pm 30\%$  band (Fig. 1b) provides a much fuller coverage of the UV plane. The image reconstructed from the data corresponding to this coverage (provided the source brightness does not depend on the frequency) has a substantially higher quality, with a signal-to-noise ratio of more than 50 (Fig. 3b).

As said above, the MFS is strongly complicated by the spectral dependence of the source brightness. If the spectral-index distribution corresponds to the model distribution shown in Fig. 2c, but we have ignored this in the reconstruction, we obtain the image in Fig. 3c, which has an even poorer quality than the single-frequency image. Indeed, the resulting image has a signal-to-noise ratio a factor of three lower than the image in Fig. 3a. Thus, this simple experiment demonstrates that applying MFS without taking into account the spectral dependence of the source emission can result in a deterioration of the reconstruction.

Our next simulations were directly related to establishing the relationship between the MFS bandwidth and the minimum necessary number of terms in the Taylor series expansion (3) of the spectral component of the image when frequency corrections are applied. It is clear that, the wider the frequency band, the stronger the effect of the spectral component and the greater number of terms in the series required for a satisfactory correction of the images. However, it is not reasonable to include a very large number of terms in the expansion, since this results in an unjustifiably large number of unknowns in the optimization problem, which can, in turn, lead to a deterioration of the reconstruction.

Figure 4 shows the results of reconstructing the source emission distribution, first-order spectral map, and spectral-index distribution with a frequency band of  $\pm 30\%$  of the central frequency (UV coverage of Fig. 1b). According to (6), the spectral-index distribution is defined by the pixel-by-pixel division [9] of the reconstructed first-order spectral term  $I_1(x, y)$  by the reconstructed brightness  $I_0(x, y)$ , for all pixel values exceeding some empirically chosen threshold, to avoid division by zero or very small values. The spectral-index maps were all obtained with the same threshold value of 0.004 of the peak of  $I_0(x, y)$ . The upper row of maps were obtained using the first two terms in the Taylor series expansion (2), and the lower row of maps using three terms in the expansion; these two sets of results virtually coincide. A fairly high quality of the reconstruction has been achieved. Thus, the first-order spectral term is sufficient when using a fairly narrow frequency band ( $\pm 30\%$ ), consistent with the results of other studies [3–6].

Figure 5 presents the reconstruction results for a  $\pm 60\%$  frequency band (UV coverage in Fig. 1c). The upper, middle, and lower rows of the maps were obtained using the first two, three, and four terms in expansion (3). Using the first-order spectral term alone does not yield a satisfactory quality of the reconstruction, while using the third-order spectral term is unnecessary, since the results using the second term along and both the second and third terms virtually coincide. Thus, using a frequency band of up to 60% requires including higher-order terms together with the first-order spectral term. Addition of the second-order spectral term approximately doubles the resulting signal-to-noise ratio.

Figure 6 shows the reconstruction results for a much broader frequency band reaching  $\pm 90\%$  of the central frequency (UV coverage in Fig. 1d). The rows of maps from top to bottom were obtained using the first two, three, four, and five terms in expansion (3). Including only the first-order spectral term in the spectral correction is clearly not sufficient. Including the second-order spectral term appreciably improves the quality of the reconstruction, increasing the signal-to-noise ratio by almost a factor of two. Including the third-order spectral term provides a further substantial improvement in the quality of the reconstruc-

tion, increasing the signal-to-noise ratio by another factor of 1.5. Including the fourth-order spectral term results in a further, though not so significant, improvement in the quality of the reconstruction. Thus, using a frequency band of up to 90% requires taking into account spectral terms at least up to third order.

The results of our simulations demonstrate that the highest accuracy of the reconstruction can be achieved for the  $I_0(x, y)$  source images, while the maps of the first-order spectral term  $I_1(x, y)$  have a lower accuracy, and the spectral-index maps  $\alpha(x, y)$  have the lowest accuracy. In particular, the maximum signal-to-noise ratios achieved for the  $I_0(x, y)$ ,  $I_1(x, y)$ , and  $\alpha(x, y)$  maps are 40, 15, and 4, respectively

An intercomparison of the best reconstruction results obtained using each frequency band demonstrates that, for the same number of frequencies within the band, the quality of the reconstruction degrades slightly with increasing bandwidth. This is true because, with increasing frequency bandwidth, we must increase the number of spectral terms taken into account. In turn, for the same number of visibility measurements, the number of unknowns in the optimization of (25) is increased. To improve the reconstruction quality of images with increasing frequency bandwidths, we must proportionally increase the number of frequencies in the band. The simulations demonstrate (Fig. 7) that using 27 (instead of 9) frequencies in a  $\pm 90\%$  band increases the signal-to-noise ratio to 54 and the image dynamic range to 3200.

Figure 8 shows the reconstruction results obtained from data containing appreciable errors. The dynamic range of the maps obtained is reduced by approximately a factor of four due to the effect of the errors. The contour levels on these images are 0.25, 0.5, 1, 2, 4, 8, 16, 32, 64, and 99% of the peak value. Figure 8a presents the radio map reconstructed from single-frequency data (Fig. 1a), which displays a higher level of distortion than the analogous map in Fig. 3a. Figure 8b shows the MFS map obtained using a  $\pm 90\%$  band with nine frequencies (Fig. 1d), neglecting the spectral dependence of the source emission. This map is likewise characterized by strong distortions, and its signal-to-noise ratio is only 1.4, a factor of six lower than the previous map. Figures 8c, 8d, 8e, and 8f present MFS maps reconstructed from the same data including two, three, four, and five terms in the expansion (2), respectively. Adding subsequent terms to the expansion substantially improves the quality of the reconstruction. The inclusion of spectral terms up to fourth order improves the signal-to-noise ratio to 20, twice the signal-to-noise ratio in the data. Figures 8g and 8h show the maps of the first-order spectral term and the spectral index reconstructed using five terms in expansion (2). The spectral-index map was obtained using (7) with a threshold value of 0.01 of the peak in the  $I_0(x, y)$  map. The signal-to-noise ratios of the spectral-term and spectral-index maps are six and two, respectively. A comparison of these images with the model maps indicates a satisfactory reconstruction of the source intensity (the dynamic range is about 400) and spectral-index distributions, even in the presence of a considerable noise in the data. The quality of the reconstruction is substantially improved by increasing the number of frequencies within the frequency band. In particular, if the number of frequencies is tripled, the dynamic range of the maps is approximately doubled.

## 6. CONCLUSION

Multifrequency synthesis is an effective means of synthesizing the aperture of a radio interferometer, which can enable high-dynamic-range imaging of radio sources. The main problem that must be solved in MFS is the need to apply a frequency correction to the

images, due to the frequency dependence of the source brightness. Deconvolution algorithms incorporating such a frequency correction based on the CLEAN method are well known. The best studied of these is a double-deconvolution algorithm intended for linear spectral correction. This algorithm is effective when applied to frequency bandwidths no broader than  $\pm 30\%$ .

We have proposed, developed, and studied a more fundamental deconvolution method for MFS images based on a generalized maximum entropy method. This new method makes it possible to apply frequency corrections in a much broader frequency band, due to the ability to include non-linear terms of arbitrary order, together with the linear term of the spectral component of the image. The main advantage of MEM over CLEAN – the ability to more accurately restore extended sources – is also realized. In addition, the developed algorithm enables acceptably accurate estimation of the spectral-index distribution.

Our numerical simulations have enabled us to establish regularities in the quality of the image reconstruction associated with changes in the frequency bandwidth, number of frequencies within the frequency band, number of spectral terms included, and the noise level in the input data. We conclude that our developed deconvolution method with frequency correction is most effective for mapping extended sources in a broad frequency band using high-precision visibility data. The proposed spectral correction method can be further developed using the principle of difference mapping [19], intended to improve the quality of image reconstruction for sources whose structure includes both compact and extended components. Another subject of further studies is a combination of MFS with phaseless mapping [20], including also data from a high-orbit space radio interferometer [21].

#### ACKNOWLEDGMENTS

This work was supported by the Basic-Research Program of the Presidium of the Russian Academy of Sciences on The Origin and Evolution of Stars and Galaxies and the Program of State Support for Leading Scientific Schools of the Russian Federation (grant NSH-6110.2008.2, "Multi-wavelength Astrophysical Research"). The author thanks the referee for valuable comments, which helped to improve the paper.

#### REFERENCES

1. A. R. Thompson, J. M. Moran, and G. W. Swenson, *Interferometry and Synthesis in Radio Astronomy*, (Wiley, New York, 1986; Fizmatlit, Moscow, 2003).
2. A. T. Bajkova and A. M. Finkelstein, *Astron. Astrophys. Trans.* **1**, 159 (1992).
3. J. E. Conway, T. J. Cornwell, and P. N. Wilkinson, *Mon. Not. R. Astron. Soc.* **246**, 490 (1990).
4. J. E. Conway, *ASP Conf. Ser.* **19**, 171 (1991).
5. R. J. Sault and M. H. Wieringa, *Astron. Astrophys. Suppl. Ser.* **108**, 585 (1994).
6. R. J. Sault and J. E. Conway, in: *Synthesis imaging in Radio Astronomy II*, eds G. B. Taylor, C. L. Carilli, R. A. Perley, *ASP Conf. Ser.* **180**, 419 (1999).
7. R. J. Sault and T. A. Oosterloo, e-Print arXiv:astro-ph/0701171v1 (2007).
8. J. A. Högbom, *Astron. Astrophys. Suppl. Ser.* **15**, 417 (1974).
9. S. F. Likhachev, V. A. Lodynin, and I. A. Girin, *Izv. Vyssh. Uchebn. Zaved., Ser. Radiofiz.* **49**, 553 (2006).
10. B. R. Frieden, *J. Opt. Soc. Amer.* **62**, 511 (1972).

11. J. G. Ables, *Astron. Astrophys. Suppl. Ser.* **15**, 383 (1974).
12. J. Skilling and R.K.Bryan, *Mon.Not. R. Astron. Soc.* **211**, 111 (1984).
13. S. J. Wernecke and L. R. DAddario, *IEEE Trans. Comp.* **C-26**, 351 (1977).
14. T. J. Cornwell and K. F. Evans, *Astron. Astrophys.* **143**, 77 (1985).
15. R. Narayan and R. Nityananda, *Ann. Rev. Astron. Astrophys.* **24**, 127 (1986).
16. T. J. Cornwell, R. Braun, and D. S. Briggs, in: *Synthesis imaging in Radio Astronomy II*, eds G. B. Taylor, C. L. Carilli, R. A. Perley, *ASP Conf. Ser.* **180**, 151 (1999).
17. A. T. Bajkova, *Rep. Institute Appl.Astron.No. 58 (Inst. Appl. Astron. Ross. Akad. Nauk, S.-Petersburg, 1993)*.
18. B. R. Frieden and A. T. Bajkova, *Appl. Opt.* **33**, 219 (1994).
19. A. T. Bajkova, *Astron. Zh.* **84**, 984 (2007) [*Astron. Rep.* 51, 891 (2007)].
20. A. T. Bajkova, *Pisma Astron. Zh.* 30, 253 (2004) [*Astron. Lett.* **30**, 218 (2004)].
21. A. T. Bajkova, *Astron. Zh.* **82**, 1087 (2005) [*Astron. Rep.* 49, 947 (2005)].

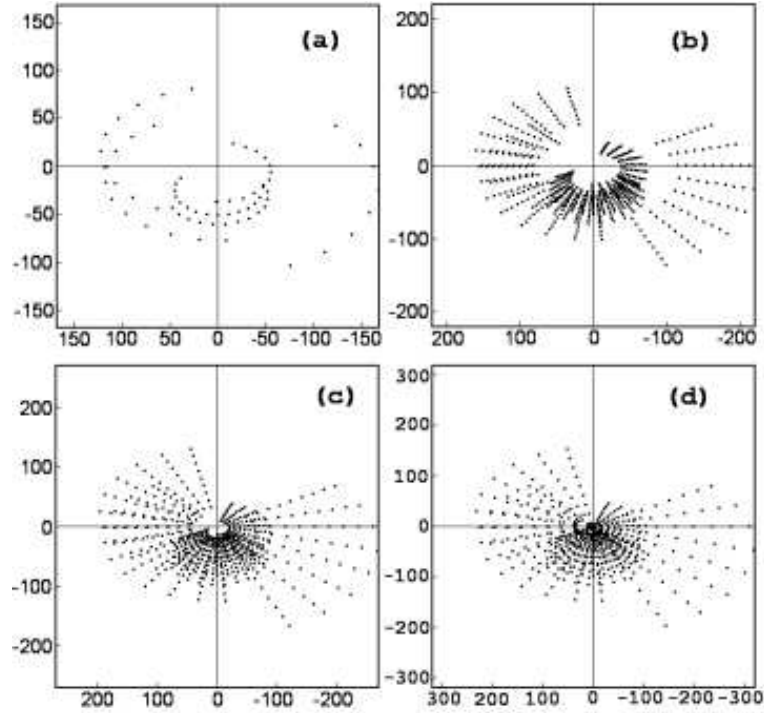


Fig. 1.  $UV$  coverages for a four-element radio interferometer comprised of the Svetloe, Zelenchukskaya, Badary, and Matera stations for a 12-hour observation of a radio source with a declination of  $34^\circ$ , for (a) single-frequency observations ( $\nu_0 = 8.2$  GHz) and multi-frequency synthesis in a band encompassing (b)  $\pm 30\%$ ,  $\pm 60\%$ , and (d)  $\pm 90\%$  of the reference frequency (nine frequency channels are used in each band). The horizontal and vertical axes show the  $U$  and  $V$  spatial frequencies in millions of wavelengths.

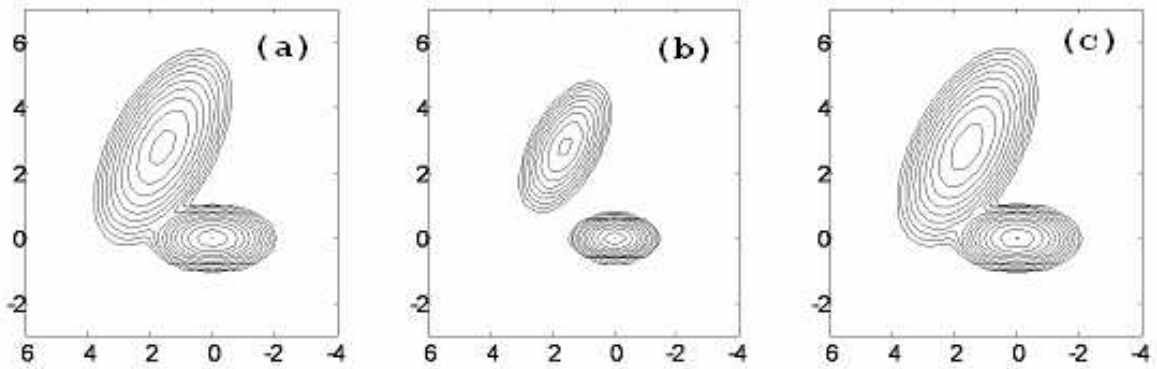


Fig. 2. Model (preset) (a) radio intensity map  $I_0(x, y)$ , (b) first-order spectral map  $I_1(x, y)$ , and (c) spectral-index map  $\alpha(x, y)$ . The horizontal and vertical axes plot right ascension  $x$  and declination  $y$  in milliarcseconds.

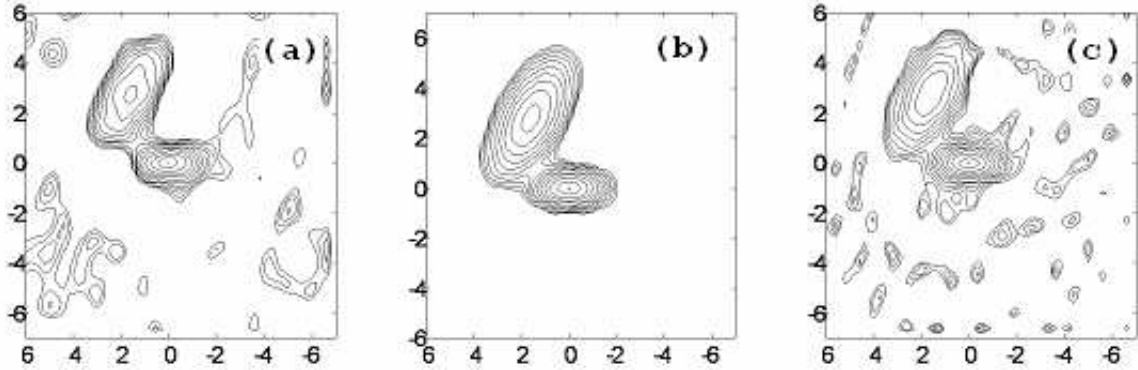


Fig. 3. Restored maps of the radio source using (a) single-frequency data, (b) MFS data in a  $\pm 30\%$  band assuming frequency independence of the image ( $\alpha(x, y) = 0$ ), and (c) from MFS data in the same band without assuming frequency dependence of the image ( $\alpha(x, y) \neq 0$ ).

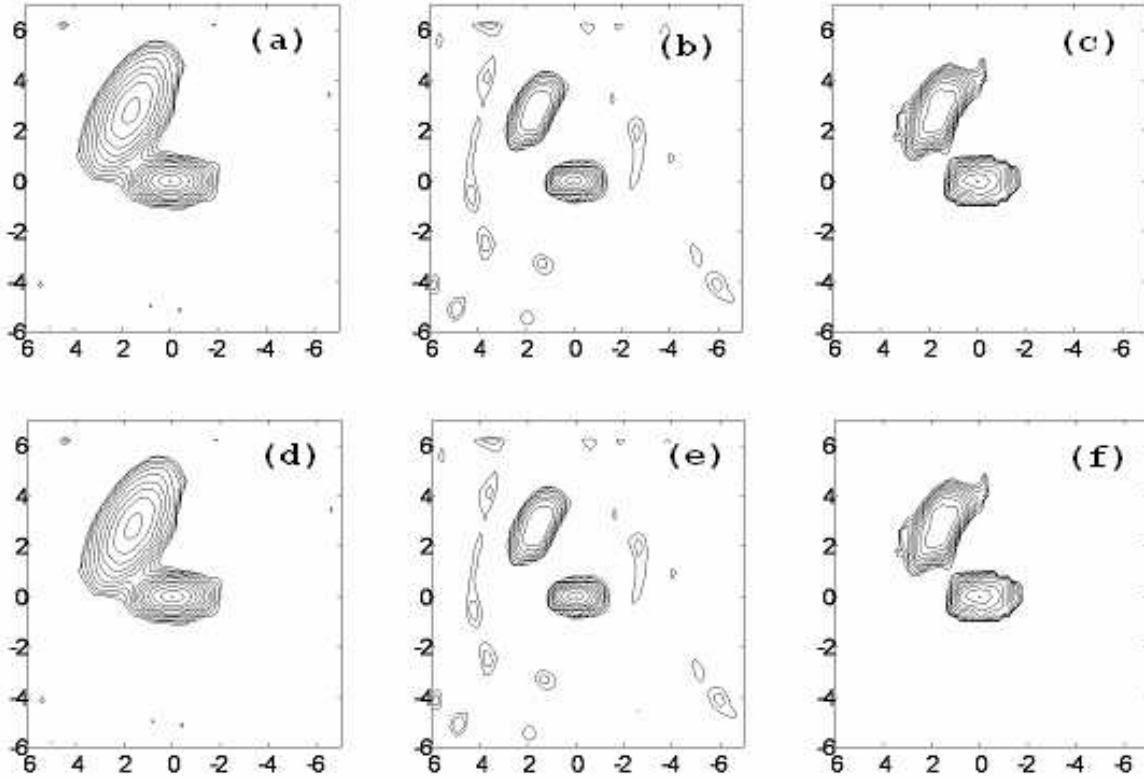


Fig. 4. Results of the reconstruction using MFS data in a  $\pm 30\%$  band. The horizontal ordering of the maps is as in Fig. 2. Maps of the upper row (a), (b), (c) were obtained using the first two terms, and maps of the lower row (d), (e), (f) the first three terms of the Taylor series expansion.

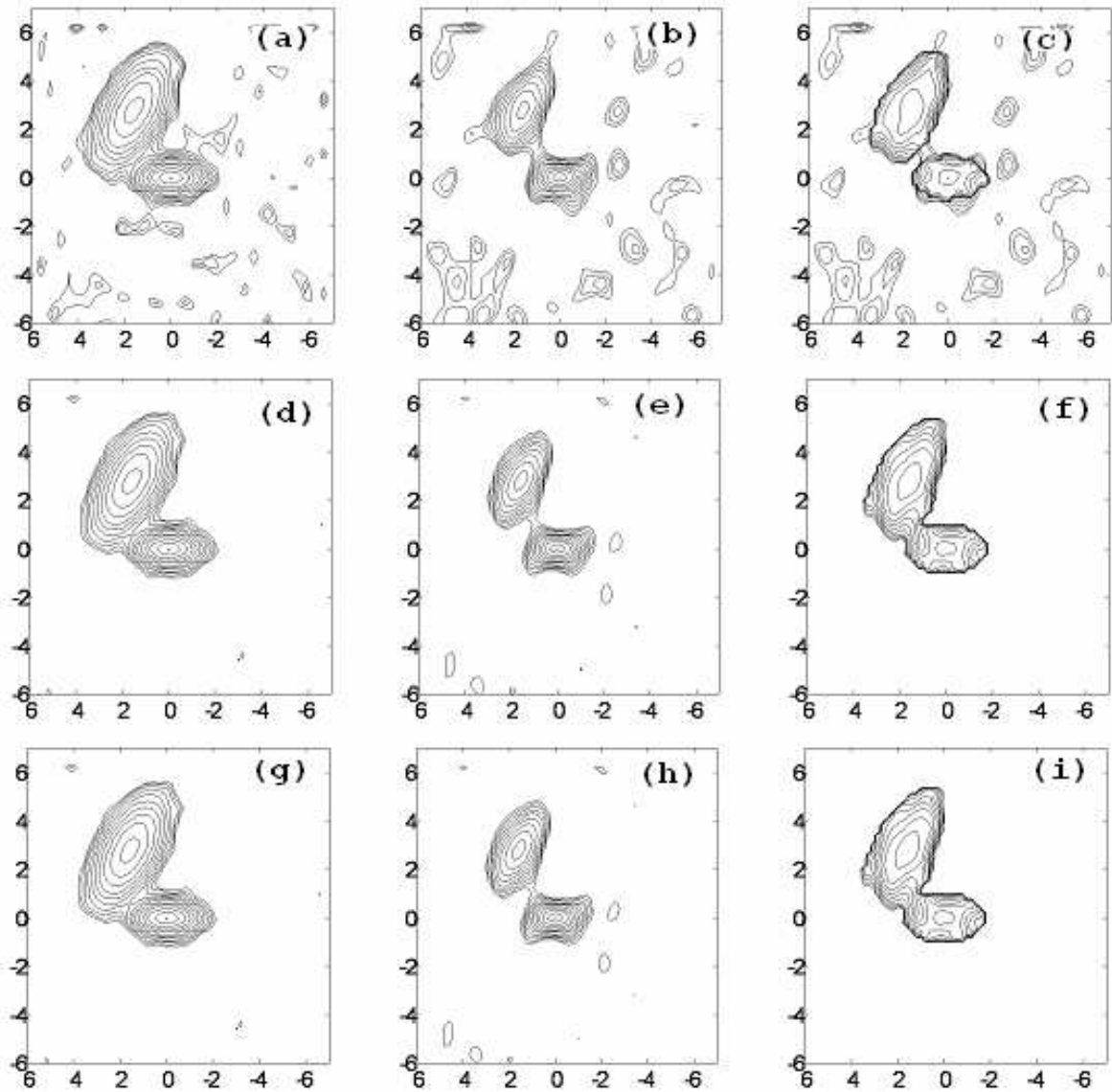


Fig. 5. Results of the reconstruction using MFS data in a  $\pm 60\%$  band. The horizontal ordering of the maps is as in Fig. 2. Maps of the upper row (a), (b), (c) were obtained using the first two terms, maps of the middle row (d), (e), (f) the first three terms, and maps of the lower row (g), (h), (i) the first four terms of the Taylor series expansion.

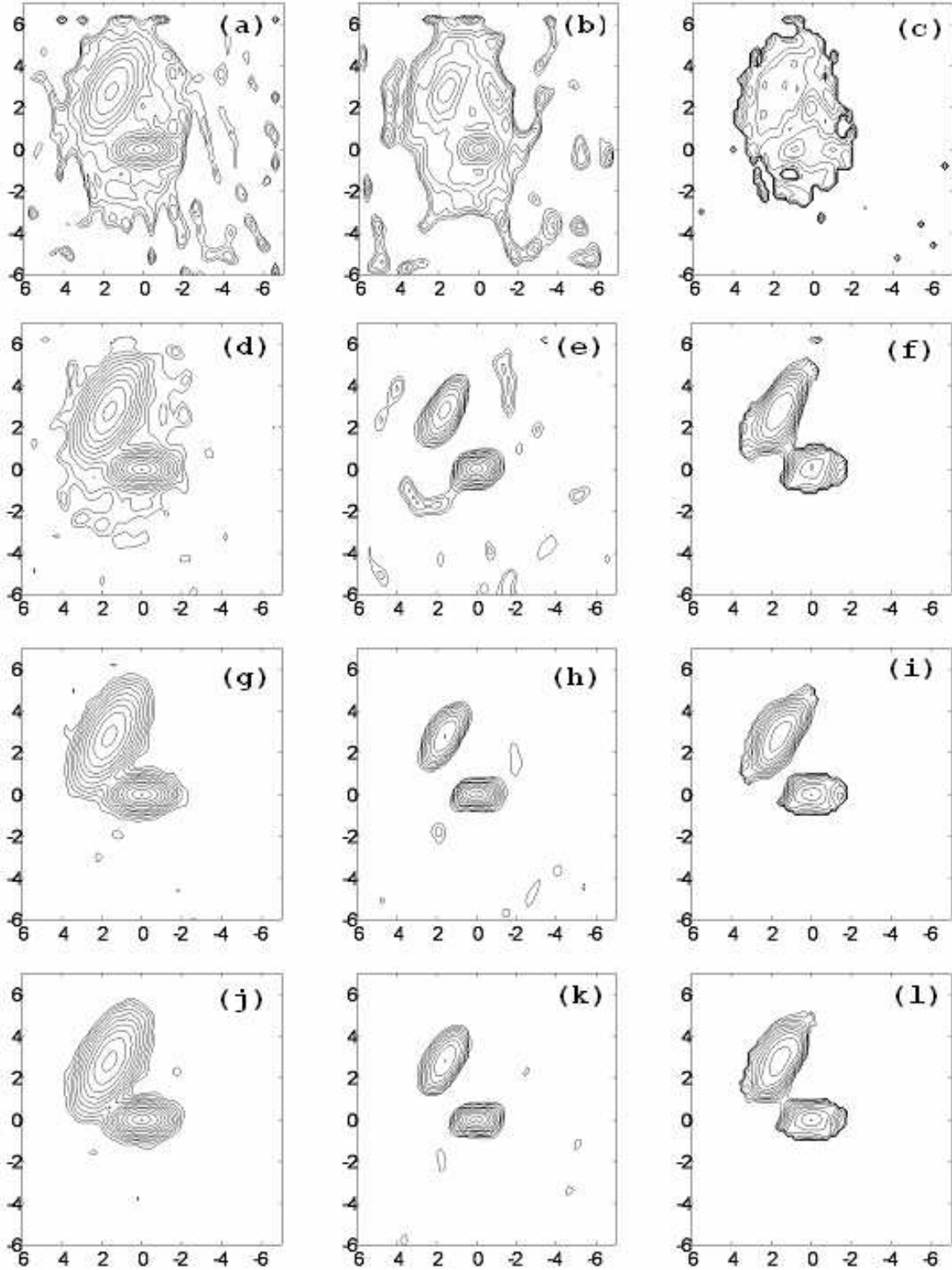


Fig. 6. Results of the reconstruction using MFS data in a  $\pm 90\%$  band. The horizontal ordering of the maps is as in Fig. 2. Maps of the first row (a), (b), (c) were obtained using the first two terms, maps of the second row (d), (e), (f) the first three terms, maps of the third row (g), (h), (i) the first four terms, and maps of the fourth row (j), (k), (l) the first five terms of the Taylor series expansion.

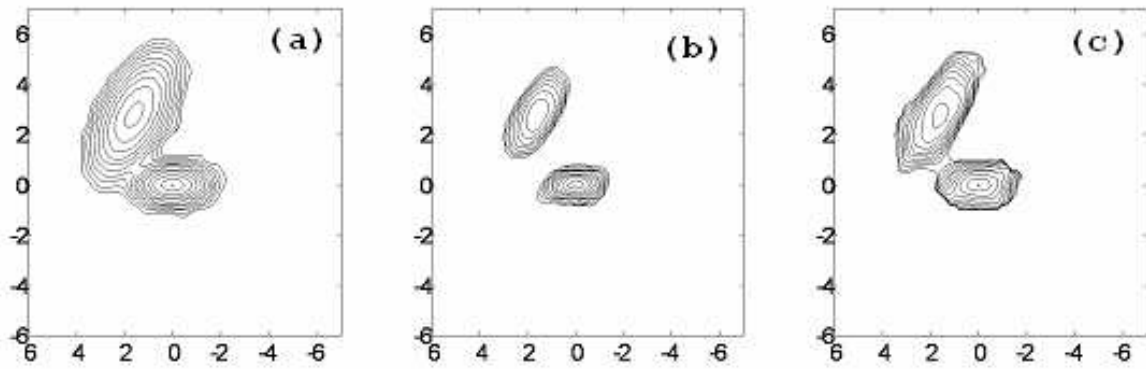


Fig. 7. Results of the reconstruction using MFS data in a  $\pm 90\%$  band with 27 frequency channels using five terms in the Taylor series expansion. The horizontal ordering of the maps is as in Fig. 2.

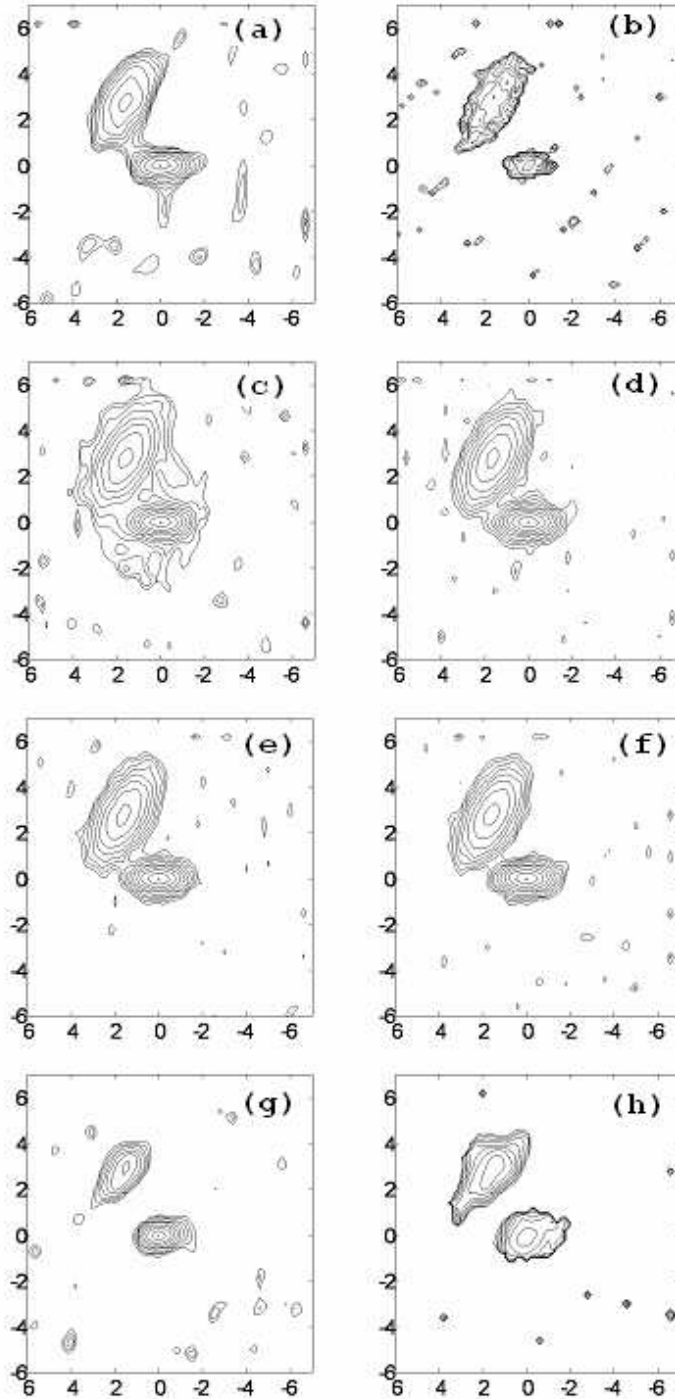


Fig. 8. Results of the reconstruction with appreciable data errors (a) for single-frequency data (UV coverage of Fig. 1a); (b) for MFS with a  $\pm 90\%$  band without assuming frequency dependence of the map. Panels (c), (d), (e) and (f) show the radio images obtained using two, three, four, and five terms of the Taylor series expansion of the spectral term, respectively, and panels (g) and (h) the first-order spectral map and spectral-index map corresponding to map (f).